Energy & Environmental Science

Accepted Manuscript

This article can be cited before page numbers have been issued, to do this please use: B. Fan, G. Liu, Y. Dai, Z. Dong, R. Luan, L. Gong, Z. Zhang, Z. L. Wang and C. Zhang, *Energy Environ. Sci.*, 2024, DOI: 10.1039/D4EE02662D.

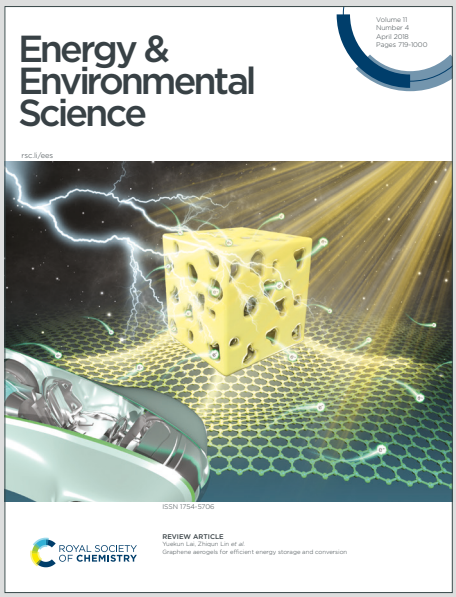




ROYAL SOCIETY OF CHEMISTRY

rsc.li/ees

View Article Online
DOI: 10.1039/D4EE02662D

# Broader context statement

As society moves into the age of the Internet of Things, Artificial Intelligence, and Big Data, wearable movable smart gadgets with smaller sizes and more complex functions are growing in popularity. It is vital to develop eco-friendly, light, durable, and adaptable flexible power sources. Fiber textile materials are commonly found in human life, and they can effectively adapt to complex deformations caused by body movement, it is an ideal carrier for collecting kinetic energy from the human body. Tribovoltaic effect is a phenomenon of the generation of direct voltage and current by the mechanical friction at semiconductor interface, hence, we present a wearable DC textile power woven by P/N-type organic semiconductor fibers based on the tribovoltaic effect. The WDPs can provide a DC output of 40 V, 2.2 mA, and its power density can reach 1.05 W/m$^2$, with excellent human morphology adaptability and long-term stability of 72,000 cycles, the WDPs can directly power electronic devices such as commercial lithium-ion batteries, mobile phone and ink electronic screens. The high-performance WDP provides a promising strategy for the practical application of tribovoltaic effect in the field of textile power supplies and smart wearable electronics.



View Article Online
DOI: 10.1039/D4EE02662D

ARTICLE

# A wearable DC tribovoltaic power textile woven by P/N-type organic semiconductor fibers

Received 00th october 20xx,
Accepted 00th october 20xx

DOI: 10.1039/x0xx00000x

Beibei Fan [a,c], Guoxu Liu [a,b], Yiming Dai [a,c], Zefang Dong [a,b], Ruifei Luan [a,b], Likun Gong [a,b], Zhi Zhang [a,b], Zhong Lin Wang [a,b,d,e], Chi Zhang [a,b,c *]

High-performance direct current (DC) textile power supply is an urgent demand for wearable electronics. Herein, we present a wearable DC textile power woven by P/N-type organic semiconductor fibers based on the tribovoltaic effect. The hydrophobic P-type semiconductor PEDOT: PF and N-type semiconductor poly(benzodifurandione) are woven into a spiral fiber (SF). By serial/parallel combination, the SFs are woven into a wearable DC textile power (WDP). The WDPs can provide a DC output of 40 V, 2.2 mA, and its power density can reach 1.05 W/m$^2$, which is approximately 75 times higher than that of previous textile triboelectric nanogenerators. With excellent human morphology adaptability and long-term stability of 72,000 cycles, the electronic devices such as commercial lithium-ion batteries, mobile phone and ink electronic screens can be directly powered the WDPs. The high-performance WDP provides a promising strategy for the practical application of tribovoltaic effect in the field of textile power supplies and smart wearable electronics.

.

## Introduction

As society moves into the age of the Internet of Things, Artificial Intelligence, and Big Data, wearable movable smart gadgets with smaller sizes and more complex functions are growing in popularity[1–3]. Theoretically, an endless, easily accessible, and eco-friendly power supply system is requisite for powering these enormous numbers of low-power wearable electronic devices[4–6]. However, rechargeable capacitors/batteries currently fall short of meeting future sustainable and environmentally acceptable energy needs due to inherent issues such as frequent charging requirements, waste disposal difficulties and safety risks[7–9]. Hence, it is vital to develop eco-friendly, light, durable, and adaptable flexible power sources. Fiber textile materials are commonly found in human life, and they can effectively adapt to complex deformations caused by body movement, it is an ideal carrier for collecting kinetic energy from the human body[10–14]. Developing smart textiles that generate electrical energy from mechanical movements is an effective approach towards the upcoming era of wearable electronics. Scientists have recently developed a variety of green and sustainable textile power sources based on piezoelectric, triboelectric, thermoelectric, photovoltaic, and electrochemical effects[11,15–20]. Among them, the biocompatible and flexible fiber-based triboelectric nanogenerators (TENGs), which can convert biomechanical kinetic energy into electrical energy, have attracted particular attention from scientists[21–29]. The TENG is based on contact electrification and electrostatic induction, however, do not match wearable smart electronics due to their high voltage, high impedance, low current density, and AC output characteristics[4,30–32]. In addition, humidity environment can cause surface charge dissipation of most fiber materials, affecting the contact electrification effect, further limiting the application of the fiber-based TENG[6,10,14,30]. The development of textile power supplies that possess characteristics such as low impedance, high DC current density and humidity resistance continues to present a noteworthy challenge[14,33–35].

Tribovoltaic effect is a phenomenon of the generation of direct voltage and current by the mechanical friction at semiconductor interface, in which the friction forms new chemical bonds to release energy called "bindington" and excite the electron-hole pairs at the semiconductor interface, thus resulting in a DC by the action of built-in electric field or interfacial electric field [36–41]. The tribovoltaic nanogenerator (TVNG) is a very promising technology for the direct conversion of mechanical energy into DC electricity in smart wearable electronics. Recently scientists have developed various power textile based on the tribovoltaic effect. Wang and Liu et al. reported a planar friction structure of Al/organic-semiconductor PEDOT:PSS fabrics, where a dynamic Schottky contact interface can generate DC electricity when the Al slides continuously on the fabric[42,43]. Due to the excellent conductivity and hydrophobicity, polypyrrole (PPy) is one of the best materials in the field of flexible electronics. Shao and Pu et al. slid (or pressed) aluminum (or gold)

Electronic Supplementary Information (ESI) available. See DOI: 10.1039/x0xx00000x

[a] CAS Center for Excellence in Nanoscience, Beijing Key Laboratory of Micro-nano Energy and Sensor, Beijing Institute of Nanoenergy and Nanosystems, Chinese Academy of Sciences, Beijing 101400, China.
[b] School of Nanoscience and Technology, University of Chinese Academy of Sciences, Beijing 100049, China.
[c] Center on Nanoenergy Research, School of Physical Science and Technology, Guangxi University.
[d] Georgia Institute of Technology, Atlanta, GA, USA
[e] Guangzhou Institute of Blue Energy, Knowledge City, Huangpu District, Guangzhou 510555, China
* Corresponding author: czhang@binn.cas.cn (C. Zhang)

View Article Online
DOI: 10.1039/D4EE03663D



on PPy conductive textile to generate direct current, and its current density has made a breakthrough[44–46]. Dong et al. developed an all fibric-based TVNG with a plane/plane friction mode, and its output characteristics were examined under various interfacial friction scenarios[47]. However, most fiber-based TVNGs are the plane/plane friction mode, which not only occupies a large space and leads to the loss of garment aesthetics, but also does not match the human body morphology movement, resulting in low energy harvesting efficiency. In addition, the lower power function difference between semiconductor interfaces causes the output voltage of TVNGs to be about 0.1-1.0 V. The fiber-based TVNGs in plane/plane friction mode would seriously undermine the portability of wearable devices. Therefore, developing textile power supplies that are comfortable to wear, form-fitting, highly moisture-resistant, mechanically robust, high voltage, high DC and low impedance remains a great challenge[4,10,13,14].

In this work, we present an organic semiconductor fiber-based wearable tribovoltaic DC textile power. The poly(3,4-ethylenedioxythiophene):perfluorinated sulfonic acid (PEDOT: PF) and poly(benzodifurandione) (PBFD) are woven into a spiral fiber (SF). By serial/parallel combination, the SFs are woven into a wearable DC textile power (WDP). The influence of diameter, mechanical stress, movement pattern (tensile state and compression states) and series/parallel parameters on the electrical output of the WDPs were systematically investigated. The open-circuit voltage ($V_{oc}$) and short-circuit current ($I_{sc}$) of WDP are 40 V and 2.2 mA respectively, and its power density can reach 1.05 W/m$^2$, which is approximately 75 times higher than that of previous textile TENGs and TVNGs. The performance of WDP does not degrade after 72,000 cycles, and it still maintains 80% output performance in the humidity environment of 90%. The WDPs still maintain 70% output performance after being washed 15 times and 117 days with no loss of performance. The WDPs achieve a 3.1-fold improvement in durability, and 11.5-fold reduction in internal resistance compared to previous textile TENGs and TVNGs, which can charge a 10 mF commercial capacitor to 5 V in 67 s and a commercial lithium-ion battery to 3 V in 55 min. The WDPs are well matched to human morphological motions and it can directly power smart devices such as mobile phones, sports wristbands and colourful electric lights when the body is in motion without power management. The high-performance WDPs demonstrated in this work provide a promising strategy for the practical application of tribovoltaic effect in the field of textile power supplies and smart wearable electronics.

## Results and Discussion

### Material design and Working mechanism

In this work, the hydrophobic P-type organic semiconductor solution (PEDOT:PF, Fig. S1A, B) and N-type organic semiconductor solution (PBFD, Fig. S1C, D) were prepared, and further two functional fibers with P-type and N-type semiconductor properties were prepared by interfacial adsorption and impregnation methods. To ensure a tight friction interface between the P-type and N-type semiconductor fibers, we employed the spiral winding method, resulting in a three-dimensional spiral structure. Fig. 1A shows the fabrication process of two semiconductor fibers. Firstly, the plasma treatment of the cotton fibers (CFs) to enhance the surface activity of CFs. For the preparation of PEDOT:PF@$Ti_3C_2$@CFs semiconductor fibers, due to the excellent conductivity and hydrophilicity, $Ti_3C_2$ offers the possibility to fabricate advanced flexible electronic materials. For making PEDOT:PF completely adsorbed on the CF surface, PEDOT:PF@$Ti_3C_2$ was firstly prepared by electrostatic self-assembly method. Firstly, the CFs were immersed into cetyltrimethylammonium bromide (CTAB) solution and sonicated for 1 h. Next, the CFs-CTAB were immersed into a multilayer $Ti_3C_2$ solution (Fig. S1E, F) for 1 h to facilitate interfacial electrostatic self-assembly. Finally, the fibers were dried under vacuum at 60 °C for 12 h to obtain the $Ti_3C_2$@CFs fibers (Fig. S2A). The polymerization process for PEDOT:PF is described briefly in Methods, wherein we utilized perfluorosulfonic acid (PF) ionomers as counterions in the alcohol phase to prepare semiconductor solutions[48]. Following that, the $Ti_3C_2$@CFs fibers were directly immersed into the PEDOT:PF solution, continuously stirred for 2 hours, and finally vacuum-dried at 60°C for 12 hours to achieve PEDOT:PF@$Ti_3C_2$@CFs semiconductor fibers (Fig. S2B). For the preparation of PBFD@CFs semiconductor fibers, the CFs fibers were stirred in the PBFD solution at 50°C for 6 hours, followed by vacuum drying at 50°C for 24 hours. By doing so, PBFD@CFs semiconductor fibers were obtained (Fig. S2C). To complete the process, both the PEDOT:PF@$Ti_3C_2$@CFs semiconductor fibers and PBFD@CFs semiconductor fibers were woven into a three-dimensional single helical structure using the helical winding method (Fig. S3)[49–51]. In Fig. 1B, the X-ray diffraction (XRD) pattern displays characteristic peaks that confirm the successful synthesis of both PEDOT:PF@$Ti_3C_2$@CFs semiconductor fibers and PBFD@CFs semiconductor fibers. In the case of PEDOT:PF@$Ti_3C_2$@CFs semiconductor fibers, the sharp (002) peak at 13.5º corresponds to the multilayer $Ti_3C_2$, whereas the amorphous wide peak observed in the range of 20-30º represents the composite of CFs and PEDOT:PF. On the other hand, the peak (100) at 7.9º in the XRD pattern of PBFD@CFs semiconductor fibers indicates the characteristic peak of PBFD[52]. These XRD results further support the successful synthesis of the desired semiconductor fibers.

The work function of semiconductor heterojunction interface materials significantly influences their electrical properties. Consequently, the work functions of PBFD and PEDOT:PF with different molar ratios is investigated. In Fig.1C, the work function of the N-type PBFD is 4.6 eV. In contrast, the work function of the P-type PEDOT:PF increases as the ratio of anti-ionic PF rises. When the PEDOT to PF ratio is 1:2, the work function reaches 4.9 eV, while a ratio of 1:8 results in a work function of 5.7 eV (Fig. S4). A higher work function in PEDOT:PF facilitates the formation of upward band bending at the interface when in contact with the polymer donor, enhancing efficient hole collection. Moreover, a larger work function difference at the interface contributes to improved interface barrier and increased $V_{oc}$[34,41,43]. Fig. 1D illustrates the *I-V* characteristics of PBFD/PEDOT:PF (1:8) at the heterogeneous interface under mechanical pressure ranging from 1 to 100 N. The *I-V* curves exhibit a typical Schottky contact, introducing a strong internal electric field at the interface, which is a key factor in the manufacture of high-performance TVNGs.

The working mechanism of TVNG with PBFD/PEDOT:PF Schottky contact is based on the tribovoltaic effect, as shown in Fig. 1E-F. In the sliding mode, the work function of PBFD is lower than that of PEDOT:PF before the contact. When PBFD and PEDOT:PF come into contact, electrons transfer from PBFD to PEDOT:PF, aligning their Fermi energy levels. This generates a built-in electric field ($E_b$) at the PBFD/PEDOT:PF interface, forming a space charge layer.

Consequently, the energy levels of PEDOT:PF (the conduction band) bend downwards at the interface. During the sliding process, the mechanical energy produced by friction separates the electron-hole pairs at the interface. Electrons are excited into the conduction band, while large number of holes remain in the valence band. As depicted in Fig.1G, under the influence of $E_b$, electrons flow from PEDOT:PF to PBFD, and holes flow in the opposite direction, resulting in a continuous DC. In addition, previous studies have shown that the induced electric field ($E_{CE}$) generated by contact electrification can also affect the movement of heterojunction charge carriers[43,47,53]. To obtain the direction of the $E_{CE}$, the change of surface potential of PEDOT: PF during the friction process between PEDOT: PF and PBFD were investigated, as shown in Fig. S5. The surface of PEDOT: PF was negatively charged, indicating the presence of contact electrification. The direction of the $E_{CE}$ was directed from PBFD to PEDOT: PF. The electric fields $E_b$ and $E_{CE}$ are in the same direction, and the carriers move in one direction in the superposition of $E_b$ and $E_{CE}$. The charge distributions and electrostatic potentials of the two semiconductor molecules from separation state to contact state were further simulated by molecular dynamics as in Fig.1H-J and Fig. S6. As shown in Fig.1H and I, when the two semiconductors are in an independent state, in the PEDOT:PF molecular system, the -$CF_3$ group exhibits the strongest electronegativity and the C-C ring structure exhibits the strongest positive electronegativity, and in the PBFD molecular system, the consecutive benzene ring structure exhibits positive electronegativity and the C=O group exhibits electronegativity. When the two molecules come into contact, -$CF_3$ PEDOT:PF in exhibits the greatest negative potential, and the benzene ring structure in PBFD exhibits the greatest negative potential, showing that PBFD tends to be positively charged and PEDOT:PF tends to be negatively charged (Fig. J).

Some work has shown that in the compression state, compression force can cause a decrease in the Schottky barrier height at the interface, and that the decrease in barrier height breaks the equilibrium and causes electrons to shift at the interface, a situation that generally requires a higher pressure[44–46]. Some previous studies have suggested that the "mechanochemical" effect arising from contact charging is likely to be the cause[54]. Specifically, when atoms at the interface of the two materials come close together, atom-atom interactions or new bonds form through overlapping electron clouds, as illustrated in the Fig. S7 model. In this process, the continuous input of frictional energy will lead to the continuous formation and breaking of chemical bonds, and the formation of chemical bonds will release an energy quantum, which is named "binding", and this energy may be large enough to excite electron-hole pairs[40,45,55]. Thus, even in the absence of strong frictional motion, "bindington" can occur under certain contact pressures. As shown in Fig.1K and L, in the sliding mode, the $V_{oc}$ generated by the PBFD/PEDOT:PF interface increases from 0.27 V to 1.1 V, and the short-current density rises from 2.8 μA/cm² to 19 μA/cm² under mechanical pressures of 1-100 N. In the compression mode, $V_{oc}$ increases from 0.2 V to 1.2 V, while the short-current density increases from 1.5 μA/cm² to 15.7 μA/cm². In addition, the types of electrode materials for this back electrode were further investigated, typically organic conducting carbon(OCC), metallic materials (Al, Ag, Au, Pt), and two-dimensional graphene(GR) were examined. As shown in Fig. S8 and S9, in both sliding and compression modes, except for the lower output performance of OCC compared to $Ti_3C_2$, the output performance of other electrode materials is close to $Ti_3C_2$. $Ti_3C_2$ has a great potential in the field of flexible electronics due to its high electrical conductivity, excellent mechanical properties and solution processability, we further compared the tensile-strain characteristics of semiconductor fibers at different electrodes. As shown in Fig. S10, the PEDOT:PF@$Ti_3C_2$@CFs exhibits optimal tensile flexibility in P-type organic semiconductor fibers.

Based on the above DC output characteristics of the PBFD/PEDOT:PF interface, the electrical output of the single SF is further investigated. The influence of fiber diameter and excitation frequency on the electrical output of SFs in the compression and tensile states were investigated. As shown in Fig. M-P, Fig. S11, the $V_{oc}$ and $I_{sc}$ of SFs in the tensile state (30% strain) increased with increasing diameter and frequency, the $V_{oc}$ is 0.18 V and $I_{sc}$ is 1.5 μA at 0.2 mm,1 Hz, and further increases to 1.29 V and 11.2 μA as the diameter increases to 10 mm and the frequency increases to 5 Hz. The tensile strain of this SFs and the electrical output at different strains were further investigated. As shown in the Fig. S12, the maximum strain of SFs is about 87% and the $V_{OC}$ and $I_{SC}$ increase from 0.37 V and 2.5 μA at 10 % strain to 1.1 V and 9.3 μA at 80 %. In the compression state, as shown in the Fig. S13, the $V_{oc}$ is 0.11 V and $I_{sc}$ is 2 μA at 0.2 mm,1 Hz, and further increases to 1.2 V and 11.1 μA as the diameter increases to 10 mm and the frequency increases to 5 Hz (It should be noted that, if not otherwise stated, 2 mm CFs were selected for this study).

**Series/Parallel characteristics and Weaving design**

At present, the fiber-based TVNGs face several challenges. The current designs utilize a metal-Al/fabric or fabric/fabric two-plane friction structure (Fig. 2A (i) and (ii)). However, this design is bulky, compromises clothing aesthetics, and is difficult to integrate into wearable electronic devices, thus limiting normal human activity. Furthermore, the existing TVNGs based on Al/fabric or fabric/fabric interaction have limited output voltages (0.1-1.0 V) and currents (μA-level current) and can only harvest energy from one sliding direction. To enable a larger-scale application of fiber-based TVNGs on the human body, a three-dimensional TVNG with the following characteristics is required: high shape adaptability, excellent stability, high voltage (≥ 5 V), mA-level current, all-round energy harvesting, and easy integration (Fig. 2A (iii)). To fabricate this textile power source, as shown in Fig. 2B-D, analogous to a conventional battery structure, a single three-dimensional SF was assembled in series or parallel to investigate the $V_{oc}$ and $I_{sc}$ of the assembled textile. For the series connection of 1-50 sections of SFs, as shown in Fig. 2E-F, the $V_{oc}$ of the textile increases from 0.45 to 24.5 V and the $I_{sc}$ increases from 3.5 to 4.5 μA in the tensile state. As shown in Fig. 2G-H, the $V_{oc}$ of the textile increases from 0.5 to 23 V and the $I_{sc}$ increases from 3.5 to 4.6 μA in the compression state. Similarly, in the case of a parallel connection of 1-50 sections of SF, as shown in Fig. 2I-J, the $V_{oc}$ of the textile increases from 0.55 to 1.1 V and the $I_{sc}$ increases from 4 to 176 μA in the stretched state. As shown in Fig. 2K-L, the $V_{oc}$ of the textile increases from 0.58 to 0.88 V and the $I_{sc}$ increases from 4.5 to 170 μA in the compression state. In summary, as shown in Fig. S14, it can be concluded that series connection has a more pronounced effect on the $V_{oc}$ of the assembled textile, and parallel connection has a more pronounced effect on the $I_{sc}$ of the assembled textile, which is

consistent to the series-parallel characteristics of commercially available batteries. Based on the series/parallel electrical properties of SFs, as shown in Fig2. M and Fig. S15, in this study, 5 series SFs are used as a base assembly unit (5S-SF), and 5S-SF × 5S-SF parallel structure is used as a sub-assembly unit (25SP-SF), and the SFs are woven into a wearable DC textile power source through traditional weaving process and layer-by-layer assembly strategy (WDP). As shown in Fig. 2N (i)-(iv), the WDP has a double-layer structure that exhibits excellent flexibility and tensile properties.

View Article Online
DOI: 10.1039/D4EE03662D

View Article Online
DOI: 10.1039/D4EE02662D





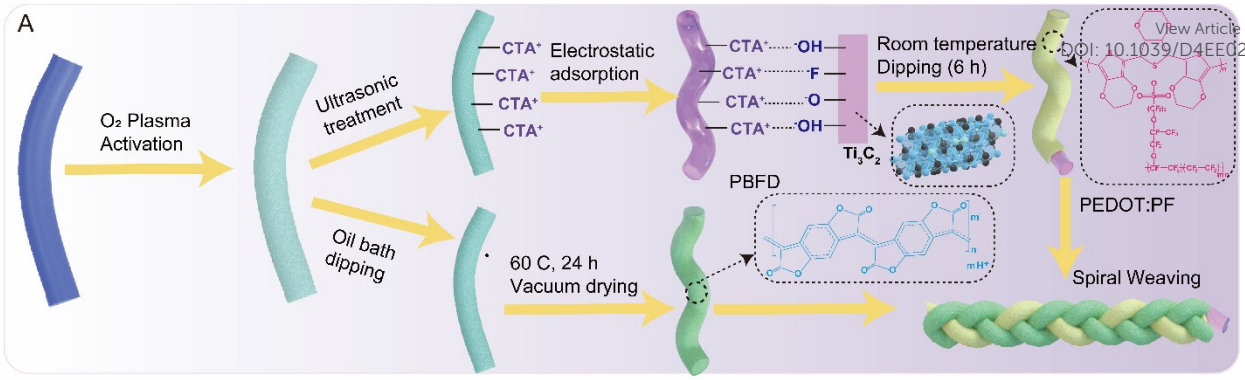


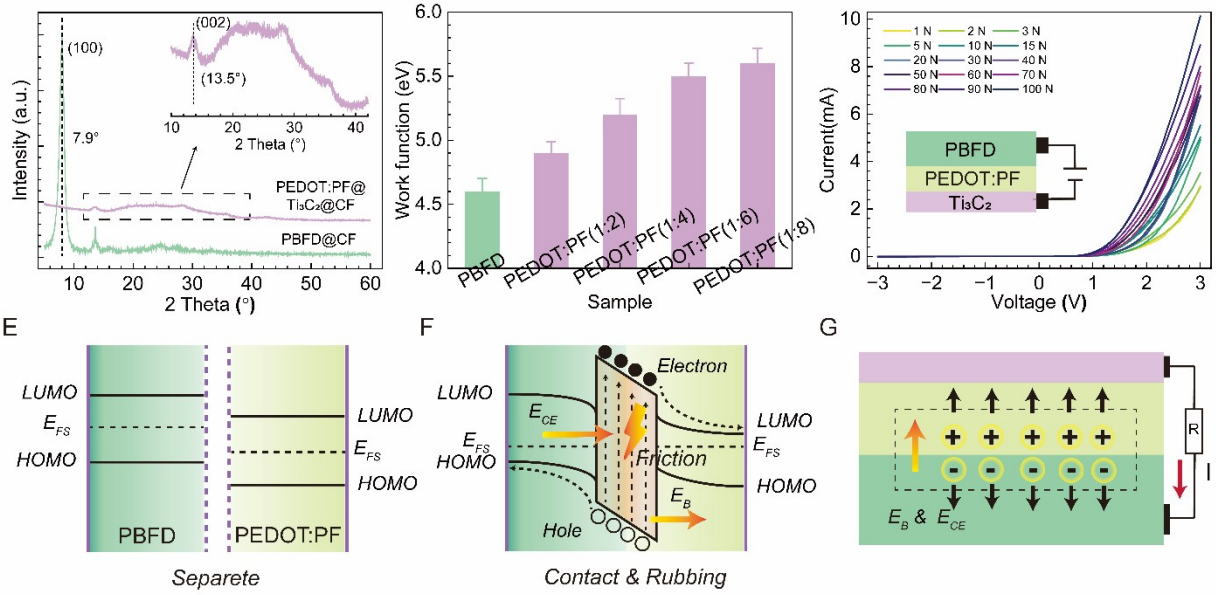





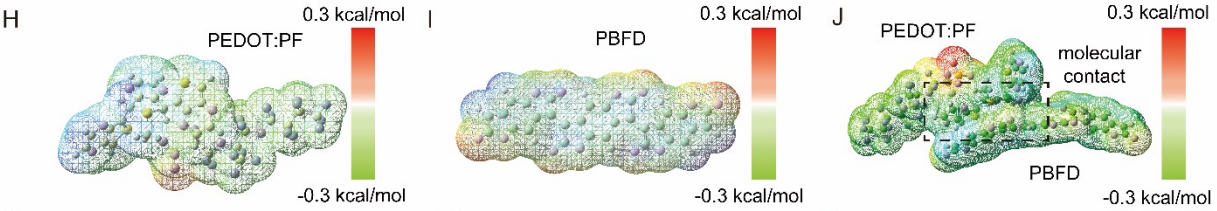


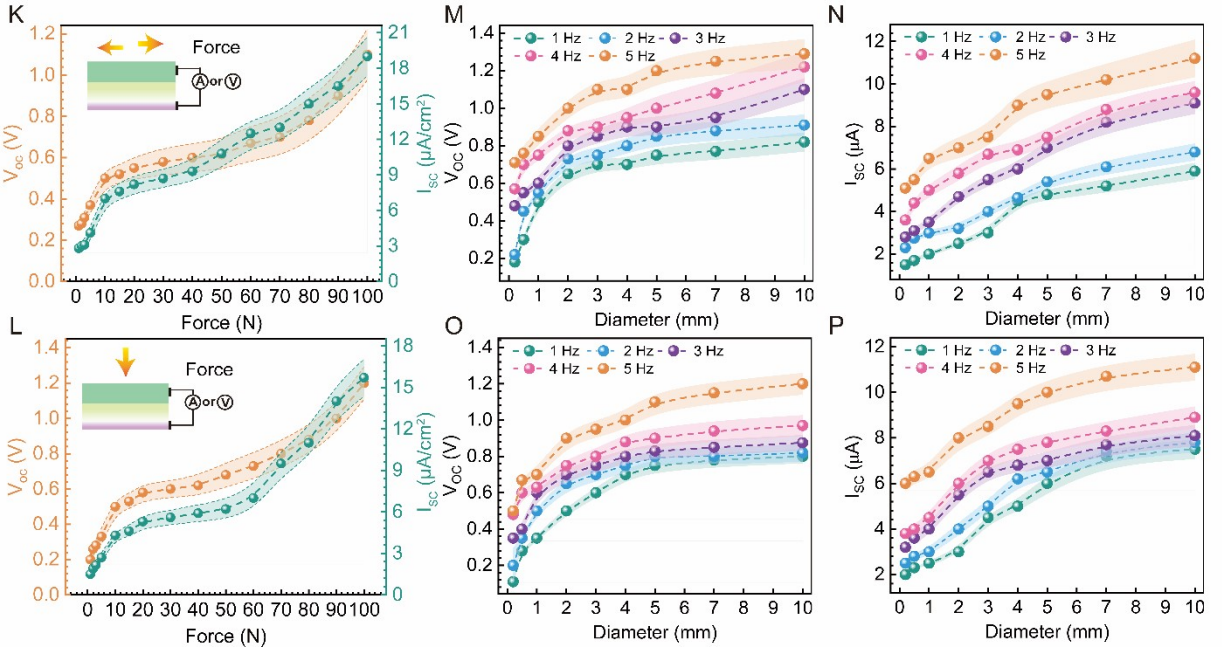

View Article Online
DOI: 10.1039/D4EE03662D

**Fig. 1. Material design and Working mechanism.** (A) Schematic illustration of of PEDOT:PF@$Ti_3C_2$@CFs, PBFD@CFs and SFs. (B) XRD patterns of PEDOT:PF@$Ti_3C_2$@CFs and PBFD@CFs. (C) Work function of PEDOT:PF@$Ti_3C_2$@CFs and PBFD@CFs. (D) *I–V* characteristic of the PEDOT:PF/PBFD heterojunction. (E-G) energy band diagram from the Separate state to Rubbing state, changes in energy levels and charge distribution. (H-J) Differential charge distribution based on molecular dynamics simulations. (K, L) $V_{oc}$ and $I_{sc}$ of sliding mode and compression mode generated by PEDOT:PF/PBFD interface. (M-P) $V_{oc}$ and $I_{sc}$ of SFs under different diameter and frequency.

.

View Article Online
DOI: 10.1039/D4EE02662D





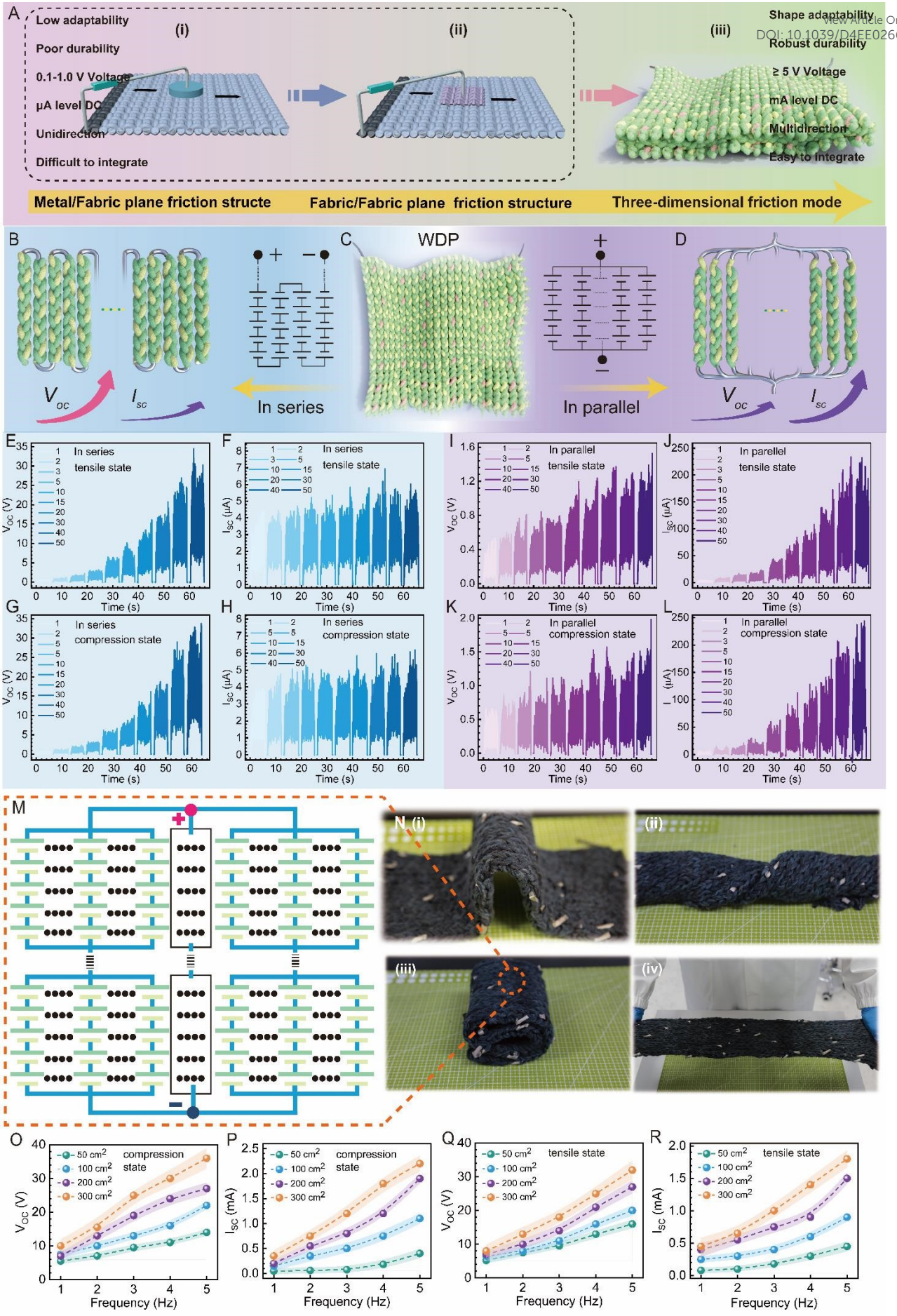

View Article Online
DOI: 10.1039/D4EE02662D

**Fig. 2. Series/Parallel characteristics and Weaving design.** (A) Advantages of 3D friction model compared with plane friction model. (B-D) Schematic diagram of SFs series and parallel connections. (E-H) Electrical properties of SFs in series. (I-L) Electrical properties of SFs in parallel. (M-N) Design structure and optical photos of WDPs. (O-R) $V_{oc}$ and $I_{sc}$ of SFs under different area and frequency.

More importantly, this dual-layer three-dimensional textile DC power source based on series/parallel combination mode has friction interfaces on the upper and lower surfaces of the textile and inside the textile compared to the plane/plane friction mode, which results in not only more friction contact sites, but also the ability to collect energy in three spatial directions, up and down, left and right, and front and back (Fig. S16).For a wearable tribovoltaic power textile, the high voltage is more favorable for it to power a wide range of electronic devices, as shown in the figure below (*Fig. S16*), compared to the friction of a single fiber in SFs, a single fiber in the 3D WDP has more friction contact sites, which will result in a higher $V_{OC}$ and power output. On the other hand, the series mode in WDP with the double-layer structure further facilitates its $V_{oc}$ increase.

In this study, the WDPs with areas of 5×10 $cm^2$, 10×10 $cm^2$, 10×20 $cm^2$ and 10×30 $cm^2$ are woven respectively, and the $V_{oc}$ and $I_{sc}$ of WDPs under the low frequency excitation of 1-5 Hz were further investigated. For quantitative characterization, a linear motor with a mechanical drive kit was used to simulate linear mechanical motion. Fig. 2 O and P show that, under cyclic compression motion, as the frequency increases from 1 Hz to 5 Hz, for the 10×30 $cm^2$ WDPs, the $V_{oc}$ increases from 10 to 40 V, the $I_{sc}$ increases from 0.4 to 2.2 mA (Video. S1 and S2). Fig. 2Q and R shows that, under cyclic tensile motion, as the frequency increases from 1 Hz to 5 Hz, the $V_{oc}$ increases from 8 to 32 V, the $I_{sc}$ increases from 0.45 to 1.8 mA (Detailed $V_{oc}$ and $I_{sc}$ for the other areas are recorded in Figure. S17 and S18).

**Electrical output and Robustness of WDPs**

Power density is an important metric for evaluating the WDPs. Herein, the 10×30 $cm^2$ WDPs were selected as the investigation object. As in Fig. 3A and C, the corresponding current magnitudes were obtained by externalizing different resistors, and the current in the loop decreases as the resistance increases. The output power density of the WDPs was further obtained by the formula: $P_d=I^2R/S$ (Where $P_d$ is the power density, $I$ is the current, $R$ is the resistance and $S$ is the fabric area). The maximum power density increased from 0.065 W/$m^2$ at 1 Hz to 1.05 W/$m^2$ at 5 Hz at a load resistance of about 35k Ω in the compression state and the maximum power density increased from 0.08W/$m^2$ at 1 Hz to 0.96 W/$m^2$ at 5 Hz at a load resistance of about 35k Ω in the tensile state (Fig. 3B and D). Based on the high output power density of WDPs, as shown in Fig. 3E and F, where the capacitors or batteries were connected in series with the WDPs while a voltmeter was connected in parallel to detect the voltage of the devices. Capacitors of 1, 2.2, 3.3, 4.7 and 10 mF were continuously charged by the WDPs, and the capacitors of 1, 2.2, 3.3, 4.7 and 10 mF reached 5 V in 8.1 ,17, 22.5 ,28, and 67 s, respectively. We charged commercial energy storage devices such as capacitors and lithium-ion batteries at 5 Hz, more importantly, the power generated by the WDPs at 5 Hz could charge a 8 mAh commercial lithium-ion battery to 3.1V in 55 minutes (Fig. 3F and S19, Video. S3). Due to the excellent morphological adaptability and wearability of WDP, it is worn on the body to obtain human movement energy to charge the battery. As shown in Fig. S20, it can charge the battery to 3.1V in 102 minutes. The electricity generated by WDPs at 3, 4, and 5 Hz can also drive colorful electric lamps with working voltages of 25, 32, and 40 V, respectively (Fig. 3G-I, Video. S4), which provides a potential solution for them to drive high-voltage (≥ 10 V) wearable electronic devices. As a sustainable textile power source, WDPs should have sufficient mechanical durability and chemical stability for practical applications, so the robustness of the textile was systematically investigated. First, the cyclic washability and long-term durability of the WDP were investigated. As shown in Fig. 3J and Fig. S21, the WDP maintained 70% of its output performance after 15 cycles of washing, and more importantly, the performance of WDP did not deteriorate after 117 days. Furthermore, the electrical output of the WDPs gradually decreases to about 80% of its original value as the relative humidity increases from 5% to 90% (Fig. S22). The increase in humidity will lead to an increase in water vapor in the environment, and a small amount of water vapor will adsorb on the surface of fibers, which will reduce the contact friction between fibers, thereby reducing the output performance of WDP. Distinguishing from the wear damage of the two planar friction modes, one of the great advantages of the WDPs is the potential long-lasting durability, and to verify this advantage, the long-term output performance of the WDPs were tested in compression and tensile motion modes as shown in Fig. 3K and Fig.S23. Obviously, the WDPs have excellent durability and their voltage did not drop significantly after 72,000 cycles. The WDPs were compared with the previously reported TENGs and TVNGs, which achieved a 75-fold increase in power density, an 11.5-fold decrease in internal resistance, and a 1.6-fold increase in durability (Fig. 3L-N, the detailed numerical parameters are recorded in Table 1).

View Article Online
DOI: 10.1039/D4EE02662D

ARTICLE





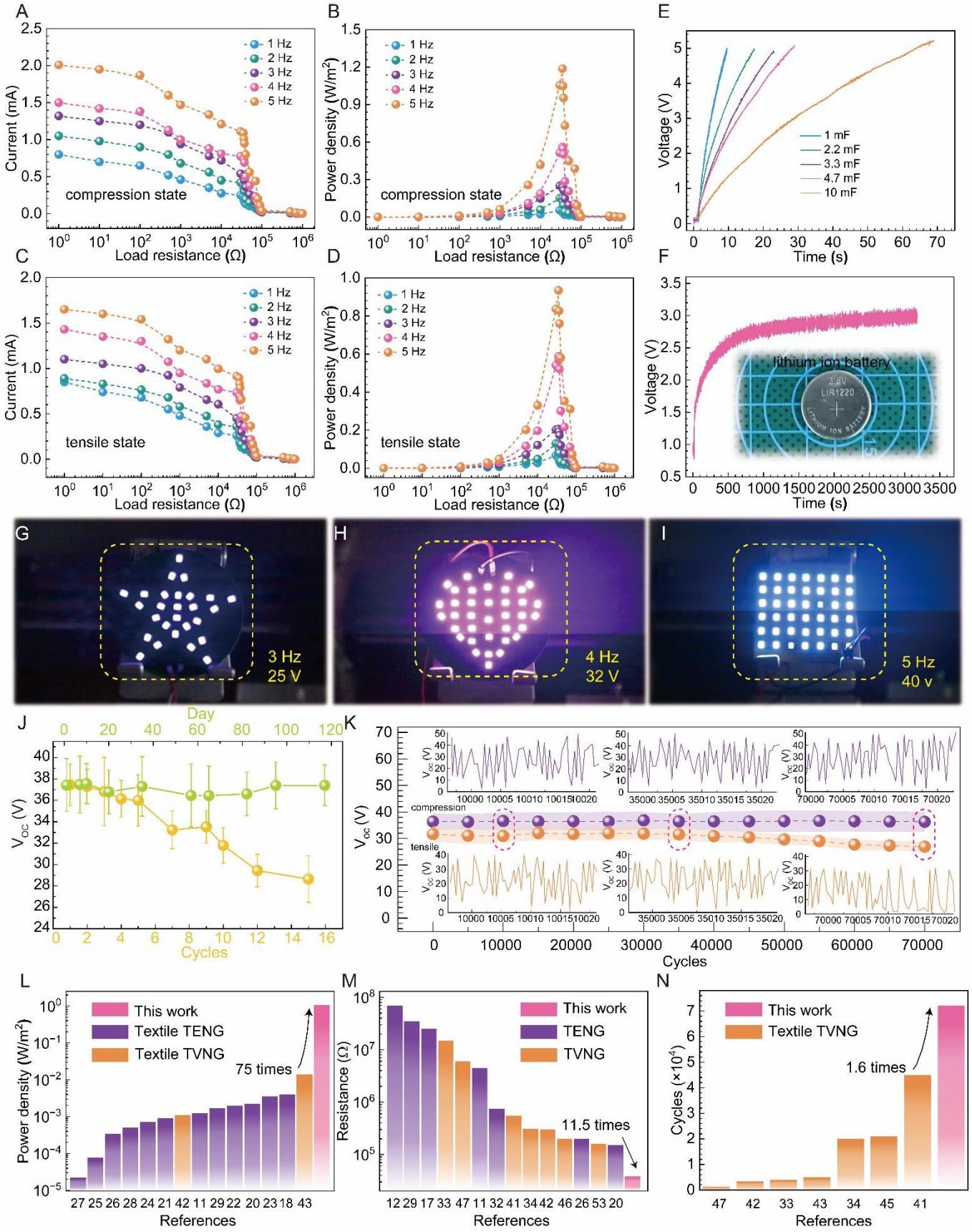

View Article Online
DOI: 10.1039/D4EE02662D

**Fig. 3. Electrical output and Durability.** (A, B) Current and power density of WDPs at different frequency in the compression state. (C, D) Current and power density of WDPs at different frequency in the tensile state. (E) Charging characteristics of WDPs with 1, 2.2, 3.3,4.7 and 10 mF capacitors. (F) Charging characteristic of WDP with a lithium-ion battery. (G-I) energy 25,32 and 40 V colorful electric lamps were directly power by WDPs at 3,4 and 5 Hz. (J) Cycle washability and long-term durability of WDPs. (K) Durability test of the WDPs. (L-M) Comparison of power density, internal resistance and durability with the previous reports.

**Prospects and Applications of WDPs**

Benefiting from the characteristics of high DC, excellent morphological adaptability, low internal resistance and environmental stability of WDPs, as shown in Fig. 4A, it has a great potential for harvesting biomechanical energy from the human body to continuously power wearable electronic devices. As shown in Fig. 4B-D, the WDPs were fixed on the elbow, knee, and feet of the human body and they match the movement of the human body shape. The WDPs generate $V_{oc}$ of 10, 7, 2.5 V and $I_{sc}$ of 0.6, 0.5 and 0.14 mA on the elbow, knee, and feet of the human body, respectively. Furthermore, the colored lights with 3, 10 and 20 V working voltage are continuously powered by the WDPs by harvesting human biomechanical energy, and due to the relatively high $V_{oc}$ of the WDPs, the bright light of the colored lights can be observed even in non-dark environments (Fig. 4E-H, Video. S5). Surprisingly, under human biomechanical motion, WDPs can directly power a 25 mW commercial mobile phone, a 10 mW smart bracelet, and a 8 mW thermo-hygrometer without any power management circuitry (Fig.4I, Fig.S24, Video. S6), and the power delivered from the WDPs is also capable of charging a 1 mF commercial capacitor up to 3.0 V with about 95 s in at fast bending speeds (Fig. 4J, Fig. S25, Video. S7), the effect of charging the capacitor at different bending speeds was further investigated, as can be seen in the Fig.S25, 82 s to 3.0 V at faster bending speeds, 110 s to 3.0 V at normal bending speeds, and 175 s to 3.0 V at slower bending speeds. To further evaluate the role of WDPs as a flexible power source in the field of self-powered motion monitoring system, we designed a human motion detection system (HMDS). As shown in Fig. S26 A and B, when human walk, the voltage generated by the WDP in the sole part of the shoe is 3.5 V, and the LED of the system will not light up. When human run, the voltage generated by the WDP in the sole is 7 V and the LED of the system starts to light up. In particular, the WDP is used for powering a Bluetooth ink screen display system (BIS), Fig. 4K indicates the circuit diagram of the BIS, which consists of a circuit management, a storage capacitor, a bluetooth transmitting system (Fig. S27) and a 16×10 $cm^2$ ink electronic screen. The WDPs can continuously power both the system circuitry and ink electronic screen, as a result the BIS system can transfer English phrases, Chinese characters, ICONS and complex human body images from the bluetooth transmitting system to the e-ink screen (Fig. 4L, and Video. S8). Finally, the effect of human skin and clothing on the performance of WDPs was investigated. The WDPs were worn on human skin and on a variety of clothing materials. As shown in Fig. S28, the performance of WDP textiles on down coat is slightly higher than that on other garments such as skin and shirts, due to the fact that the elasticity of down coat is more sensitive to forces due to the other garments, and the performance of WDP textiles in noise is also slightly higher than that in quiet environments due to the tiny vibrations caused by the environment.

View Article Online
DOI: 10.1039/D4EE02662D





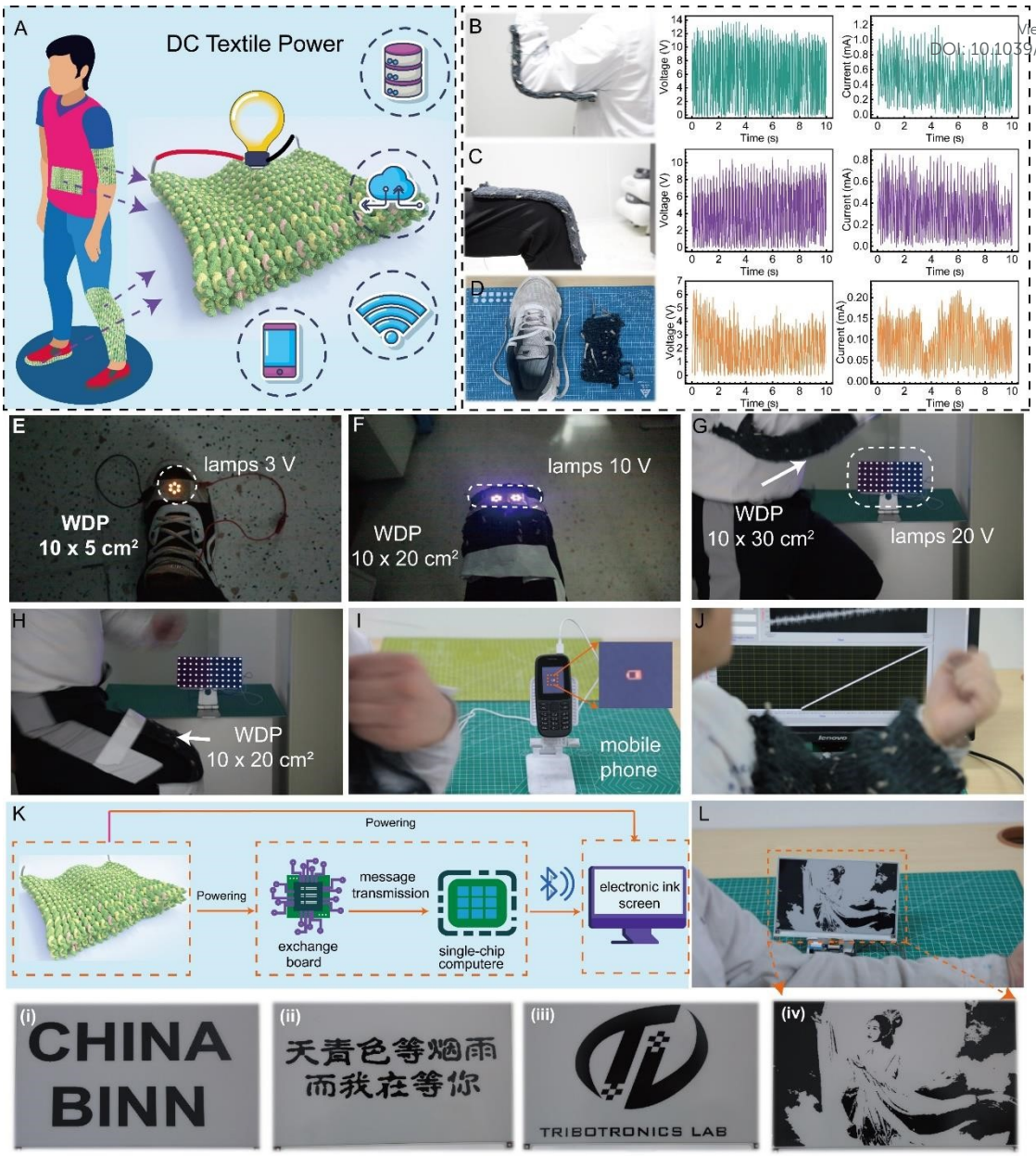


**Fig. 4 | Application and Prospect Demonstration.** (A) The outlook of WDPs in wearable electronics filed by harvesting biokinetic energies. (B-D) Demonstration of the WDPs for harvesting biomechanical energy from different parts of the human body. (E-H) Demonstration of driving 3, 10 and 20 V lamps by harvesting biokinetic energies. (I) Demonstration of directly charging a mobile phone. (J) Demonstration of directly charging 1mF capacitor. (K, L) Demonstration of directly powering 1mF capacitor a bluetooth circuit and the 16×10 $cm^2$ e-ink screens system.

## Conclusions

In summary, we report a high-performance truly wearable tribovoltaic DC power supply textile based on P/N-type organic semiconductor weaving and series/parallel layer-by-layer assembly strategy. First, the single P/N-type semiconductor fibers were helically wound to obtain a 3D SF with tighter interfacial friction. Subsequently, a power textile (WDP) with morphological adaptability, mechanical flexibility and moisture resistance was manufactured by a traditional weaving process. The WDP is a two-layer interlocking structure, which is highly deformable and can be manufactured in controlled sizes. Benefiting from the series/parallel layer-by-layer assembly strategy that achieves an output power density of about 1.05 W/$m^2$ and a $V_{oc}$ of 40 V. Compared to reported studies, the WDPs have high flexibility, excellent environmental robustness (72,000 cycles), lower internal resistance, high voltage and it still maintains

80% output performance in the humidity environment of 90%. The WDPs still maintain 70% output performance after being washed 15 times and 117 days with no loss of performance. The WDPs achieve a 11.5-fold reduction in internal resistance, a 1.6-fold increase in durability compared to previous textile TENGs and TVNGs. For a wearable textile device, the WDPs achieve an 8-fold increase in $V_{oc}$ compared to previous textile TVNGs. The WDPs can charge a 10 mF commercial capacitor to 5 V in 67 s and a commercial lithium-ion battery to 3 V in 55 min and the DC generated by WDPs from human body is enough to power lamps with 3, 12 and 20 V working voltage. The wearable WDPs are well adapted to the biomechanical movements of the human body and are easy to integrate into wearable and portable electronics, this textile can generate enough electricity for various practical applications, including light colored lights with different voltages, continuously driving mobile phones, smart electronic meters, temperature and humidity meters, and supplying power to Bluetooth transmission systems and a 16×10 $cm^2$ ink electronic screens. This hybrid textile can be widely used not only in self-powered electronics but also for larger scale DC power generation. The high-performance WDPs demonstrated in this work provides a promising strategy for the practical application of tribovoltaic effect in the field of textile power supplies and smart wearable electronics.

## Methods

**Fabrication of the PEDOT:PF:** The PEDOT:PF was synthesized via oxidation chemical polymerization. First, 10 mL of aqueous PF ionomer dispersion and 0.1 g of PEDOT were mixed in 20 ml of deionized water, followed by vigorous stirring for 2 h to form emulsion. Then 0.2 g $FeCl_3$ was added as an oxidizing agent, and after continuous stirring at 20 °C for 24 h, the obtained polymer dispersion was purified with a semi-permeable membrane, and the residual oxidizing agent and PEDOT were removed. After purification, the dark blue aqueous dispersion was then centrifuged. The resulting product was dispersed in ethanol. By adjusting the molar ratio of PEDOT to PF ionomer, PEDOT:PF with different molar ratios were obtained.

**Fabrication of the $Ti_3C_2$, $Ti_3C_2$@CFs and PEDOT:PF@$Ti_3C_2$@CFs:** The $Ti_3AlC_2$ powder was immersed into a 50% HF solution and stirred at 25 °C for 24 h. Then the resulting multilayer $Ti_3C_2$ nanosheets were obtained by centrifuging and ultrasonicating the HF-etched $Ti_3C_2$ nanosheets. Cotton fibers (CFs) were plasma treated for 10 min in an $O_2$ atmosphere, then the fibers were ultrasonically modified in 1.0 mg/mL cetyltrimethylammonium bromide (CTAB) solution for 15 min to obtain CF- CTAB composite fibers. Finally, the CF-CTAB was immersed in the prepared 5 mg/mL multilayer $Ti_3C_2$ solution for 2 h, and then vacuum dried at 60 °C for 12 h to obtain $Ti_3C_2$@CF composite fibers. The $Ti_3C_2$@CF was immersed in PEDOT:PF solution for 4 h (1 cm of PEDOT:PF@$Ti_3C_2$ was reserved as the electrode interface), and subsequently vacuum-dried at 60 °C for 12 h to obtain PEDOT:PF@$Ti_3C_2$@CF semiconductor fibers.

**Fabrication of PBFD and PBFD @CFs:** PBFD solutions were prepared according to reported methods. Briefly, PBFDs were obtained by oxidative polymerisation and in situ reductive doping processes in the presence of a quinone oxidising agent using 3,7-dihydrobenzo [1,2-b:4,5-b '] difuran-2,6-dione as the precursor. Different quinones, including dubiquinone and idebenone, were employed to obtain PBFD solutions. For the preparation of PBFD@CFs semiconductor fibers, the CFs were first plasma-treated for 5 min in an $O_2$ atmosphere, and then the CFs were further immersed into the PBFD solution with continuous stirring at 60 °C for 2 h, and then vacuum-dried at 50°C for 24 h to obtain PBFD@CF semiconductor fibers.

**Weaving strategy for the WDPs:** For the preparation of SF, as shown in Figure FS3, a 40 cm of PEDOT:PF@$Ti_3C_2$@CFs were first bent and folded in half, and the bend was fixed and knotted with one end of a 20 cm of PBFD@CF (1 cm of the knotted end of the PBFD@CF was reserved for the interface of the electrode). Subsequently, the knotted end was fixed to a textile support, the three fibers at the open end were helically wound, and finally the open end of the fiber helix was knotted to form the SF (1 cm of the open end of the PEDOT:PF@$Ti_3C_2$@CFs was reserved as the interface of the electrode). The 5S-SF was fabricated by sequentially connecting the positive and negative electrode interfaces reserved in the SF. For the preparation of the WDP, the positive electrode of the 1st 5S-SFs was firstly fixed with the middle of the 1, 2 pillars of the elliptical bracket, followed by winding the 5S-SFs along the path of the outer ends of the 1, 3, 5, 7 pillars, further winding the 5S-SFs along the path of the outer ends of the 8, 6, 4, 2 pillars, and finally reserving the negative electrode of the 5S-SFs at the outer ends of the pillars. The positive electrode of the 2nd 5S-SFs is fixed with the middle of the 7, 8 pillars of the elliptical support, and the winding process is reversed from the path of the first one, and finally the fibers of the 1st one at the outer end of the 1, 3, 5, 7 and 2, 4, 6, 8 pillars are turned away from the top to the inner end to hold down the 2nd 5S-SFs. The same process is repeated in this way with the subsequent odd numbered 5S-SFs and the even numbered 5S-SFs, in order to prepare the double-layer WDPs.

**Characterization:** Plasma treatment was carried out by a SUNJUNE PLASMA VP-R5 in $O_2$ atmosphere. Sample was characterized utilizing X-ray diffraction (XRD, Cu Kα, λ = 0.154 nm, 40 kv, 40 mA). Work function of sample were measured by KPFM (Bruker Dimension FastScan Multimode8). The *I-V* curve was measured by a Keithley 2612b. Electrical performance was measured by a low-noise electrometer (Keithley 6514, USA). Surface morphology of sample were characterized by Field Emission Scanning Electron Microscope (SEM, SU8020, Hitachi, Japanese).

**DFT:** The geometry of all molecules was optimized by density functional theory (DFT). All the DFT computations were performed by the M06-2X density functional method. The def2-SVP basis set was used for geometry optimization. All structures were generated using CYLview. All these calculations were performed with Gaussian 16 software package, the molecular distance between PBFD and PEDOT:PF is 2.48 angstroms.

## Author contributions:

Conceptualization: BBF,

Methodology: BBF, CZ, RFL

Investigation: BBF, ZFD, YMD

Visualization: BBF, GXL, RFL, LKG
Supervision: GXL, CZ
Writing—original draft: BBF, CZ, ZLW
Writing—review & editing: CZ, ZLW
Software: BBF, LKG, ZZ
Editing: BBF, LKG
All the authors discussed the results and commented on the manuscript.

## Conflicts of interest

The authors declare no competing financial interest.

## Acknowledgements

The authors thank the support of the National Natural Science Foundation of China (Nos. 52450006, U23A20640, 62104020), and Beijing Natural Science Foundation (No. 3232019).

## Notes and references

1 X. Zhao, H. Askari and J. Chen, *Joule*, 2021, **5**, 1391–1431.
2 Q. Zhang, C. Xin, F. Shen, Y. Gong, Y. Zi, H. Guo, Z. Li, Y. Peng, Q. Zhang and Z. L. Wang, *Energy Environ Sci*, 2022, **15**, 3688–3721.
3 Q. Shi, B. Dong, T. He, Z. Sun, J. Zhu, Z. Zhang and C. Lee, *InfoMat*, 2020, **2**, 1131–1162.
4 R. Liu, Z. L. Wang, K. Fukuda and T. Someya, *Nat Rev Mater*, 2022, **7**, 870–886.
5 J. Wang, S. Li, F. Yi, Y. Zi, J. Lin, X. Wang, Y. Xu and Z. L. Wang, *Nat Commun*, 2016, **7**, 12744.
6 S. Zhang, M. Chi, J. Mo, T. Liu, Y. Liu, Q. Fu, J. Wang, B. Luo, Y. Qin, S. Wang and S. Nie, *Nat Commun*, 2022, **13**, 4168.
7 A. J. Bandodkar, S. P. Lee, I. Huang, W. Li, S. Wang, C.-J. Su, W. J. Jeang, T. Hang, S. Mehta, N. Nyberg, P. Gutruf, J. Choi, J. Koo, J. T. Reeder, R. Tseng, R. Ghaffari and J. A. Rogers, *Nat Electron*, 2020, **3**, 554–562.
8 B. Dunn, H. Kamath and J.-M. Tarascon, *Science (1979)*, 2011, **334**, 928–935.
9 L. Yin, J.-M. Moon, J. R. Sempionatto, M. Lin, M. Cao, A. Trifonov, F. Zhang, Z. Lou, J.-M. Jeong, S.-J. Lee, S. Xu and J. Wang, *Joule*, 2021, **5**, 1888–1904.
10 G. Chen, Y. Li, M. Bick and J. Chen, *Chem Rev*, 2020, **120**, 3668–3720.
11 J. Chen, Y. Huang, N. Zhang, H. Zou, R. Liu, C. Tao, X. Fan and Z. L. Wang, *Nat Energy*, 2016, **1**, 16138.
12 K. Dong, X. Peng, J. An, A. C. Wang, J. Luo, B. Sun, J. Wang and Z. L. Wang, *Nat Commun*, 2020, **11**, 2868.
13 A. Libanori, G. Chen, X. Zhao, Y. Zhou and J. Chen, *Nat Electron*, 2022, **5**, 142–156.
14 H. H. Shi, Y. Pan, L. Xu, X. Feng, W. Wang, P. Potluri, L. Hu, T. Hasan and Y. Y. S. Huang, *Nat Mater*, 2023, **22**, 1294–1303.
15 Y. Jing, J. Luo, X. Han, J. Yang, Q. Liu, Y. Zheng, X. Chen, F. Huang, J. Chen, Q. Zhuang, Y. Shen, H. Chen, H. Zhao, G. J. Snyder, G. Li, T. Zhang and K. Zhang, *Energy Environ Sci*, 2023, **16**, 4334–4344.
16 S. J. Kim, J. H. We and B. J. Cho, *Energy Environ Sci*, 2014, **7**, 1959.
17 M. Li, H.-W. Lu, S.-W. Wang, R.-P. Li, J.-Y. Chen, W.-S. Chuang, F.-S. Yang, Y.-F. Lin, C.-Y. Chen and Y.-C. Lai, *Nat Commun*, 2022, **13**, 938.
18 J. Yi, K. Dong, S. Shen, Y. Jiang, X. Peng, C. Ye and Z. L. Wang, *Nano-micro Lett*, 2021, **13**, 103.
19 H. Zhang, Z. Wang, H. Li, M. Salla, Y. Song, S. Huang, S. Huang, X. Wang, K. Liu, G. Xu, J. Huang, C.-W. Qiu and Q. Wang, *Joule*, 2023, **7**, 1515–1528.
20 M. Zhou, F. Xu, L. Ma, Q. Luo, W. Ma, R. Wang, C. Lan, X. Pu and X. Qin, *Nano Energy*, 2022, **104**, 107885.
21 M. Cheng, X. Liu, Z. Li, Y. Zhao, X. Miao, H. Yang, T. Jiang, A. Yu and J. Zhai, *Chemical Engineering Journal*, 2023, **468**, 143800.
22 R. Cheng, C. Ning, P. Chen, F. Sheng, C. Wei, Y. Zhang, X. Peng, K. Dong and Z. L. Wang, *Adv Energy Mater*, 2022, 01532.
23 I. Domingos, Z. Saadi, K. S. Sadanandan, H. A. Pocinho, D. M. Caetano, A. I. S. Neves, M. F. Craciun and H. Alves, *Nano Energy*, 2023, **115**, 108688.
24 J. Huang, S. Wang, X. Zhao, W. Zhang, Z. Chen, R. Liu, P. Li, H. Li and C. Gui, *Mater Horiz*, 2023, **10**, 3840–3853.
25 L. Ma, R. Wu, S. Liu, A. Patil, H. Gong, J. Yi, F. Sheng, Y. Zhang, J. Wang, J. Wang, W. Guo and Z. L. Wang, *Advanced Materials*, 2020, 03897.
26 L. Ma, M. Zhou, R. Wu, A. Patil, H. Gong, S. Zhu, T. Wang, Y. Zhang, S. Shen, K. Dong, L. Yang, J. Wang, W. Guo and Z. L. Wang, *ACS Nano*, 2020, **14**, 4716–4726.
27 C. Ning, K. Dong, R. Cheng, J. Yi, C. Ye, X. Peng, F. Sheng, Y. Jiang and Z. L. Wang, *Adv Funct Mater*, 2020,06679.
28 C. Wei, R. Cheng, C. Ning, X. Wei, X. Peng, T. Lv, F. Sheng, K. Dong and Z. L. Wang, *Adv Funct Mater*, 2023,03562.
29 R. Wu, S. Liu, Z. Lin, S. Zhu, L. Ma and Z. L. Wang, *Adv Energy Mater*,2022,01288.
30 B. Fan, G. Liu, X. Fu, Z. Wang, Z. Zhang and C. Zhang, *Chemical Engineering Journal*, 2022, **446**, 137263.
31 F.-R. Fan, Z.-Q. Tian and Z. Lin Wang, *Nano Energy*, 2012, **1**, 328–334.
32 W. Xu, H. Zheng, Y. Liu, X. Zhou, C. Zhang, Y. Song, X. Deng, M. Leung, Z. Yang, R. X. Xu, Z. L. Wang, X. C. Zeng and Z. Wang, *Nature*, 2020, **578**, 392–396.
33 P. Deng, Y. Wang, R. Yang, Z. He, Y. Tan, Z. Chen, J. Liu and T. Li, *Advanced Science*,2022,07298.
34 F. Jiang, G. Thangavel, X. Zhou, G. Adit, H. Fu, J. Lv, L. Zhan, Y. Zhang and P. S. Lee, *Advanced Materials*, 2023,02815.

View Article Online
DOI: 10.1039/D4EE02662D



35 G. Liu, R. Luan, Y. Qi, L. Gong, J. Cao, Z. Wang, F. Liu, J. Zeng, X. Huang, Y. Qin, S. Dong, Y. Feng, L.-B. Huang and C. Zhang, *Nano Energy*, 2023, **106**, 108075.

36 Z. L. Wang and A. C. Wang, *Materials Today*, 2019, **30**, 34–51.

37 Z. Zhang, D. Jiang, J. Zhao, G. Liu, T. Bu, C. Zhang and Z. L. Wang, *Adv Energy Mater*, 2019,03713.

38 M. Zheng, S. Lin, L. Xu, L. Zhu and Z. L. Wang, *Advanced Materials*, 2020,00928.

39 J. Liu, A. Goswami, K. Jiang, F. Khan, S. Kim, R. McGee, Z. Li, Z. Hu, J. Lee and T. Thundat, *Nat Nanotechnol*, 2018, **13**, 112–116.

40 S. Lin and Z. Lin Wang, *Materials Today*, 2023, **62**, 111–128.

41 B. Fan, Z. Wang, G. Liu, Z. Wang, X. Fu, L. Gong and C. Zhang, *Adv Funct Mater*, 2023,01821.

42 J. Meng, Z. H. Guo, C. Pan, L. Wang, C. Chang, L. Li, X. Pu and Z. L. Wang, *ACS Energy Lett*, 2021, **6**, 2442–2450.

43 R. Yang, M. Benner, Z. Guo, C. Zhou and J. Liu, *Adv Function Mater*, 2021,03132.

44 X. Ding, H. Shao, H. Wang, R. Bai, J. Fang and T. Lin, *J Mater Chem A Mater*, 2022, **10**, 13055–13065.

45 J. Meng, C. Pan, L. Li, Z. H. Guo, F. Xu, L. Jia, Z. L. Wang and X. Pu, *Energy Environ Sci*, 2022, **15**, 5159–5167.

46 H. Shao, J. Fang, H. Wang, L. Dai and T. Lin, *Advanced Materials*, 2016, **28**, 1461–1466.

47 T. Lv, R. Cheng, C. Wei, E. Su, T. Jiang, F. Sheng, X. Peng, K. Dong and Z. L. Wang, *Adv Energy Mater*, 2023, 01178.

48 Y. Jiang, X. Dong, L. Sun, T. Liu, F. Qin, C. Xie, P. Jiang, L. Hu, X. Lu, X. Zhou, W. Meng, N. Li, C. J. Brabec and Y. Zhou, *Nat Energy*, 2022, **7**, 352–359.

49 T. J. Cuthbert, B. C. Hannigan, P. Roberjot, A. V. Shokurov and C. Menon, *Advanced Materials*, 2022, 09321.

50 C. Ning, R. Cheng, Y. Jiang, F. Sheng, J. Yi, S. Shen, Y. Zhang, X. Peng, K. Dong and Z. L. Wang, *ACS Nano*, 2022, **16**, 2811–2821.

51 L. Wang, F. Wan, Y. Xu, S. Xie, T. Zhao, F. Zhang, H. Yang, J. Zhu, J. Gao, X. Shi, C. Wang, L. Lu, Y. Yang, X. Yu, S. Chen, X. Sun, J. Ding, P. Chen, C. Ding, F. Xu, H. Yu and H. Peng, *Nat Nanotechnol*, 2023, **18**, 1085–1093.

52 H. Tang, Y. Liang, C. Liu, Z. Hu, Y. Deng, H. Guo, Z. Yu, A. Song, H. Zhao, D. Zhao, Y. Zhang, X. Guo, J. Pei, Y. Ma, Y. Cao and F. Huang, *Nature*, 2022, **611**, 271–277.

53 Z. Zhang, Z. Wang, Y. Chen, Y. Feng, S. Dong, H. Zhou, Z. L. Wang and C. Zhang, *Advanced Materials*, 2022, 00146.

54 M. K. Beyer and H. Clausen-Schaumann, *Chem Rev*, 2005, **105**, 2921–2948.

55 Y. Lu, Y. Yan, X. Yu, X. Zhou, S. Feng, C. Xu, H. Zheng, Z. Yang, L. Li, K. Liu and S. Lin, *Research*, 2021,7505638.

View Article Online
DOI: 10.1039/D4EE02662D

## Data availability statements

The experimental methods of this manuscript have been described in detail in **Methods**
The PDEOT and PBFD related references described in this manuscript are **48** and **52**
The data supporting this article have been included as part of the Supplementary Information.